

This is an Open Access document downloaded from ORCA, Cardiff University's institutional repository: <https://orca.cardiff.ac.uk/id/eprint/95009/>

This is the author's version of a work that was submitted to / accepted for publication.

Citation for final published version:

Yang, Tzuhsiung, Quesne, Matthew, Neu, Heather M., Cantú Reinhard, Fabián G., Goldberg, David P. and de Visser, Sam P. 2016. Singlet versus triplet reactivity in an Mn(V)-oxo species: testing theoretical predictions against experimental evidence. *Journal of the American Chemical Society* 138 (38) , pp. 12375-12386. 10.1021/jacs.6b05027

Publishers page: <http://dx.doi.org/10.1021/jacs.6b05027>

Please note:

Changes made as a result of publishing processes such as copy-editing, formatting and page numbers may not be reflected in this version. For the definitive version of this publication, please refer to the published source. You are advised to consult the publisher's version if you wish to cite this paper.

This version is being made available in accordance with publisher policies. See <http://orca.cf.ac.uk/policies.html> for usage policies. Copyright and moral rights for publications made available in ORCA are retained by the copyright holders.



1 Singlet versus Triplet Reactivity in an Mn(V)–Oxo Species: Testing 2 Theoretical Predictions Against Experimental Evidence

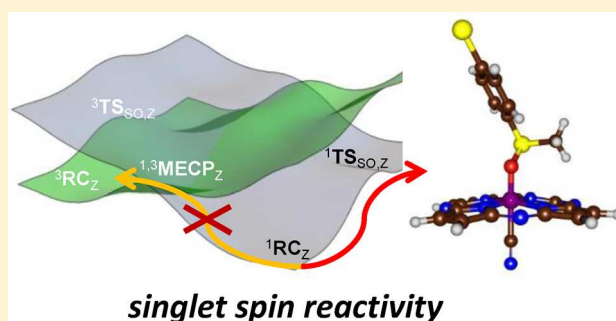
3 Tzuhsiung Yang,[†] Matthew G. Quesne,^{‡,§} Heather M. Neu,[†] Fabián G. Cantú Reinhard,[‡]
4 David P. Goldberg,^{*,†} and Sam P. de Visser^{*,‡}

5 [†]Department of Chemistry, The Johns Hopkins University, Baltimore, Maryland 21218, United States

6 [‡]Manchester Institute of Biotechnology and School of Chemical Engineering and Analytical Science, The University of Manchester,
7 131 Princess Street, Manchester M1 7DN, United Kingdom

8 **S** Supporting Information

9 **ABSTRACT:** Discerning the factors that control the reactivity
10 of high-valent metal–oxo species is critical to both an
11 understanding of metalloenzyme reactivity and related transition
12 metal catalysts. Computational studies have suggested that an
13 excited higher spin state in a number of metal–oxo species can
14 provide a lower energy barrier for oxidation reactions, leading to
15 the conclusion that this unobserved higher spin state complex
16 should be considered as the active oxidant. However, testing
17 these computational predictions by experiment is difficult and
18 has rarely been accomplished. Herein, we describe a detailed
19 computational study on the role of spin state in the reactivity of a
20 high-valent manganese(V)–oxo complex with para-Z-substituted
21 thioanisoles and utilize experimental evidence to distinguish between the theoretical results. The calculations show an unusual
22 change in mechanism occurs for the dominant singlet spin state that correlates with the electron-donating property of the para-Z
23 substituent, while this change is not observed on the triplet spin state. Minimum energy crossing point calculations predict small
24 spin–orbit coupling constants making the spin state change from low spin to high spin unlikely. The trends in reactivity for the
25 para-Z-substituted thioanisole derivatives provide an experimental measure for the spin state reactivity in manganese–oxo
26 corrolazine complexes. Hence, the calculations show that the V-shaped Hammett plot is reproduced by the singlet surface but
27 not by the triplet state trend. The substituent effect is explained with valence bond models, which confirm a change from a
28 nucleophilic to an electrophilic mechanism through a change of substituent.



29 ■ INTRODUCTION

30 Metal–oxo complexes are proposed to be the active species in
31 enzyme-catalyzed water oxidation, energy utilization, drug
32 metabolism, and many other vital functions of organisms.¹
33 One particular class of enzymes with great relevance to
34 biocatalysis and biodegradation are the cytochromes P450,
35 which in the human body have functions that give them their
36 primary purpose in the metabolism of harmful xenobiotics
37 (drugs), as well as in the synthesis of hormones.² These
38 enzymes form a high-valent iron(IV)–oxo heme cation radical
39 as the active oxidant that performs a versatile set of reactions
40 efficiently.³ While metal–oxo complexes are generally thought
41 to reside in their lower spin states in these hexacoordinated
42 heme structures, actually the iron(IV)–oxo species in
43 pentacoordinated nonheme enzymes typically exhibits a high-
44 spin state.⁴ It has been argued that the spin state of the metal–
45 oxo oxidants determines its reactivity pattern with substrates.⁵

46 Over the years a range of biomimetic model complexes have
47 been designed that mimic the active features of enzymatic
48 systems.⁶ A number of the former studies characterized an
49 active metal–oxo oxidant, which is often found in an
50 intermediate-spin iron(IV)–oxo or low-spin manganese(V)–

51 oxo state.^{7,8} It has been proposed from computational studies
52 that in many cases the active species that reacts with substrates
53 is, in fact, an excited high-spin state of the metal–oxo species
54 generated from spin crossover from the lower spin ground
55 state.⁹ This proposal arises because the excited high-spin state is
56 often calculated to give a lower energy barrier for the activation
57 of substrates, providing a possible faster reaction pathway.

58 Experimental methods to test these computational predic-
59 tions are rare. Recent work on C–H activation by nonheme
60 Fe^{IV}(O) complexes has shown that experimental kinetic isotope
61 effects (KIEs) can serve as a potential probe for the reactive
62 spin state of iron–oxo species.¹⁰ For example, very large,
63 nonclassical KIEs observed for the C–H activation reactions of
64 two nonheme Fe^{IV}(O) complexes matched calculations for the
65 lower *S* = 1 Fe^{IV}(O) spin state but did not fit for the higher *S* =
66 2 excited state. It was concluded that reactivity occurred along
67 the *S* = 1 spin state pathway, even though the quintet state was
68 calculated to yield a lower reaction barrier.^{10c} Although this
69 recent analysis of observable KIEs has provided some

Received: May 16, 2016

70 experimental measure of spin state reactivity correlations for
 71 C–H activation, an experimental test regarding spin state
 72 reactivity in the other major class of biomimetic oxidations,
 73 oxygen-atom-transfer reactions, has yet to be described. In
 74 addition, there are no reports, to our knowledge, discussing
 75 direct experimental evidence that can distinguish between
 76 possible reactive spin states in high-valent manganese–oxo, as
 77 opposed to iron–oxo, complexes.

78 Particularly useful for the studies of manganese(V)–oxo
 79 complexes are the porphyrinoid ligand systems corrole and
 80 corrolazine,^{8,11} which are able to stabilize metals in high
 81 oxidation states. Work of our groups established that a low-spin
 82 manganese(V)–oxo porphyrinoid complex $[\text{Mn}^{\text{V}}(\text{O})-$
 83 $(\text{TBP}_8\text{Cz})]$, TBP_8Cz = octakis(*p*-tertbutylphenyl) corrolazina-
 84 to^{3-} , underwent a drastic rate enhancement in hydrogen-atom
 85 abstraction reactivity upon the addition of anionic axial ligands
 86 (X^-) such as cyanide or fluoride.¹² In a separate computational
 87 study, our conclusions regarding this low-spin $\text{Mn}^{\text{V}}(\text{O})$
 88 reactivity were questioned, and it was suggested that the
 89 reactant state had a close-lying triplet spin conformation that
 90 was more likely the reactive state.¹³ A similarly large increase in
 91 reactivity for oxygen-atom-transfer (OAT) reactions was seen
 92 upon addition of X^- to $[\text{Mn}^{\text{V}}(\text{O})(\text{TBP}_8\text{Cz})]$ and reported in
 93 two separate studies.¹⁴ In one of these studies, $[\text{Mn}^{\text{V}}(\text{O})-$
 94 $(\text{TBP}_8\text{Cz})(\text{CN})]^-$ was reacted with derivatives of seven *para*-*Z*-
 95 substituted thioanisoles, and a Hammett analysis involving the
 96 measure of reaction rates versus the σ_p Hammett parameter of
 97 the *para*-*Z* substituent was conducted (lower part of Scheme
 98 1).^{14a} The obtained plot shows a surprising V-shaped pattern,

whereby a negative slope is observed for electron-donating 99
 substituents but a positive slope is seen for electron- 100
 withdrawing substituents. This observation was explained by 101
 differences in reaction mechanism, in which the former 102
 substrates reacted through an electrophilic pathway while the 103
 latter substrates reacted through a nucleophilic pathway. 104
 However, the role of spin state in these OAT reactions and, 105
 in particular, the unusual V-shaped Hammett plot was not 106
 examined in this earlier work. 107

Herein, we describe a detailed density functional theory 108
 (DFT) and ab initio study on the spin state reactivity of 109
 $[\text{Mn}(\text{O})(\text{H}_8\text{Cz})(\text{CN})]^-$ with *para*-*Z*-substituted thioanisole 110
 substrates whereby we expanded the substrate range to eight 111
 substrates (top part of Scheme 1). This study shows that the V- 112
 shaped Hammett plot provides a direct, experimental measure 113
 of the reactive spin state pathway for OAT in a high-valent 114
 manganese–oxo complex. The experimental and computational 115
 findings point to direct sulfoxidation on a dominant low-spin 116
 singlet pathway, even though an excited state triplet pathway 117
 provides an apparent lower reaction barrier. The experimentally 118
 determined Hammett plot for *p*-*Z*-thioanisole sulfoxidation by 119
 $[\text{Mn}^{\text{V}}(\text{O})(\text{TBP}_8\text{Cz})\text{X}]^-$ provides, to our knowledge, the first 120
 experimental evidence of singlet spin reactivity and the lack of 121
 spin crossing to a higher spin state surface in a high-valent 122
 manganese–oxo complex. 123

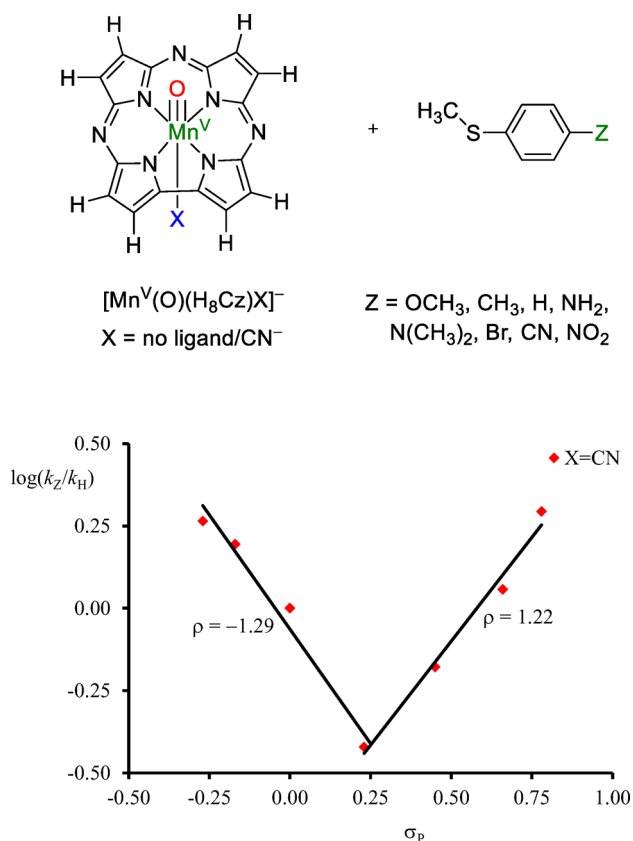
124 METHODS

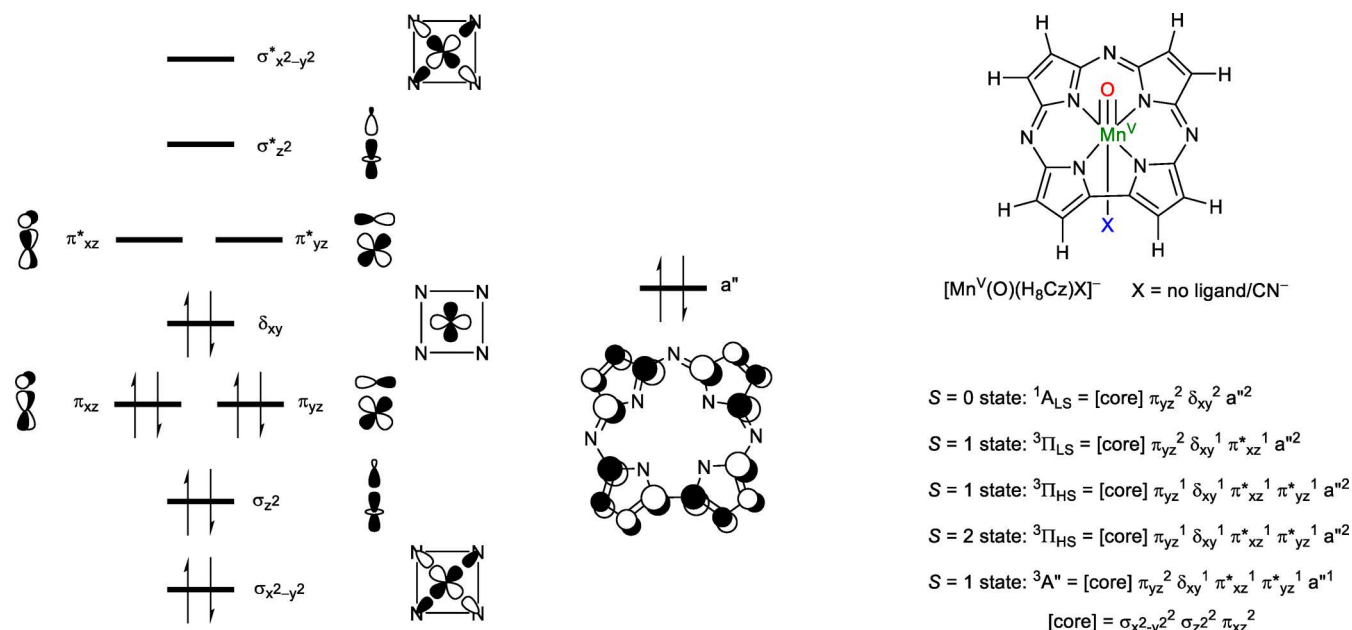
Calculations were performed using the Orca (version 3.0.3) and 125
 Gaussian-09 computational chemistry software packages.¹⁵ Our model 126
 uses a corrolazine macrocycle (Scheme 1) with the peripheral aryl 127
 substituents replaced with hydrogen atoms (H_8Cz), as previous work 128
 showed that the peripheral groups on porphyrin scaffolds have little 129
 influence on the spin state ordering and relative energies.¹⁶ Reactivities 130
 with *para*-*Z*-substituted thioanisoles were calculated for $\text{Z} = \text{N}(\text{CH}_3)_2$, 131
 NH_2 , OCH_3 , CH_3 , H , Br , CN , and NO_2 . The work was aimed at 132
 establishing whether the reaction mechanisms are electrophilic or 133
 nucleophilic and how the intrinsic chemical properties of oxidant and 134
 substrate affected these reactivity differences. The nature of all 135
 transition states, in particular, the singlet spin transition states, was 136
 established (i) through frequency calculations that gave a single 137
 imaginary mode for the S–O bond formation and (ii) intrinsic 138
 reaction coordinate (IRC) scans in both the forward and the reverse 139
 directions. The latter unequivocally connected the transition states to 140
 the reactants in one direction and to products in the opposite 141
 direction. 142

Enthalpies of activation of the chemical reactions are compared to 143
 experimental data reported previously.^{14a} However, it should be noted 144
 that generally gas-phase calculations overestimate the entropy of 145
 activation and often find higher values than experiment. As such, 146
 previous experience of calibrating oxygen transfer reactivities against 147
 low-pressure gas-phase measured rate constants gave a better 148
 correlation with enthalpies of activation,¹⁷ which we will adopt here. 149

All initial geometry optimizations (including transition state 150
 geometry optimizations) were performed without constraints and 151
 used the hybrid generalized gradient approximation (GGA) functional 152
 B3LYP that includes the VWN5 local density approximation.¹⁸ 153
 Relativistic small effective core potential basis sets SDD or LACVP 154
 were used on Mn and the all-electron 6-31G(d) on the rest of atoms: 155
 basis set BS1.¹⁹ Long-range dispersion interactions were applied using 156
 the D3 procedure of Grimme et al.²⁰ Geometry optimizations were 157
 followed by a frequency calculation at the same level of theory and 158
 confirmed all structures as local minima or first-order saddle points 159
 (transition states). Using Orca, energies were calculated from single- 160
 point calculations at the UB3LYP/BS1-optimized geometries using a 161
 correlation-consistent basis set of triple- ζ quality (cc-pVTZ) on Mn 162
 and cc-pVDZ on the rest of the atoms: basis set BS2. The resolution of 163
 identity (RI) approximation to the Coulomb integrals was used with 164

Scheme 1. Structure of Complexes and Substrates Investigated Here, and Experimental Hammett Plot with Data Taken from Ref 14a



Scheme 2. High-Lying Occupied and Virtual Molecular Orbitals of $[\text{Mn}(\text{O})(\text{H}_8\text{Cz})(\text{CN})]^-$ and Occupation Levels in Various Electronic States

165 corresponding auxiliary basis sets, as implemented in Orca. The
 166 integration grid was increased from 3 to 4 (Orca notation) to increase
 167 numerical accuracy. Single-point energy calculations on all optimized
 168 structures were also performed using the hybrid meta-GGA functional
 169 TPSSh with 10% HF exchange and the D3 dispersion correction.^{20,21}

170 A similar protocol was followed for the results obtained using the
 171 Gaussian software program, although it uses the VWN3 local density
 172 approximation in B3LYP; furthermore, these calculations utilized the
 173 triple- ζ quality LACV3P+* on the Mn (with core potential) and 6-
 174 311+G* on the rest of the atoms: basis set BS3. Generally, these
 175 studies confirmed the B3LYP obtained landscape and conclusions and
 176 did not deviate significantly. Solvent effects were included in Orca by
 177 applying the conductor-like screening model (COSMO) with a
 178 dielectric constant of 26.0 and probe radius of 1.528 Å mimicking
 179 benzonitrile.²² An implicit solvent correction in Gaussian was included
 180 using the polarized continuum model (CPCM) with a dielectric
 181 constant of $\epsilon = 35.688$ mimicking acetonitrile.

182 To test the accuracy and reproducibility of the density functional
 183 methods, a range of test calculations with alternative density functional
 184 methods and the def2-TZVPP basis set (BS4) were performed,
 185 including BP86,²³ BLYP,^{18b,23a} PBE,²⁴ B3LYP,¹⁸ PBE0,²⁵ and
 186 TPSSh.²¹ In addition, the spin state ordering of the $[\text{Mn}(\text{O})(\text{H}_8\text{Cz})-$
 187 $(\text{CN})]^-$ complex was investigated using the complete active space self-
 188 consistent field (CASCF) calculations in Orca. Dynamic correlation
 189 was recovered by following these CASCF studies with the N-electron
 190 valence second-order perturbation theory (NEVPT2) correction on
 191 the converged multiconfigurational wave functions with basis set BS5
 192 (cc-pVTZ/cc-pVDZ). Due to the size of our chemical system, the
 193 NEVPT2:CAS studies were performed at the single-point energy level
 194 on the UB3LYP/BS1-optimized geometries of the reactant complexes
 195 only. The resolution of identity approximation and the chain-of-sphere
 196 approximation (RIJCOSX) were applied to the Coulomb and
 197 exchange correlation, respectively, with density fitting auxiliary basis
 198 set corresponding to each atomic basis set throughout the calculations
 199 below.

200 Single-point energies were calculated on the triplet spin state of the
 201 optimized singlet spin transition state geometry using B3LYP. The
 202 ZORA Hamiltonian with the model potential due to Van Wullen²⁶
 203 was used to account for the relativistic effect along with the segmented
 204 all-electron relativistically recontracted version of basis sets def2-
 205 TZVPP.²⁷ The Ahlrichs (2df,2pd) polarization functions were
 206 obtained from the Turbomole basis set library²⁸ for Mn, while the

def2-SVP basis set²⁷ was employed on the rest of atoms. The
 207 resolution of identity (RI) and the chain-of-sphere approximations
 208 were used for the Coulomb and Exchange correlation, respectively.
 209 Spin-orbit coupling constants (SOC) were calculated on the
 210 converged unrestricted natural orbitals using the spin-orbit mean
 211 field Hamiltonian including 1-electron term and local DFT correlation
 212 including VWN5.²⁹ Coulomb terms were computed with the RI
 213 approximation, and the exchange terms were computed with one-
 214 center exact integrals including the spin-orbit interaction. 215

RESULTS AND DISCUSSION

216 Density functional theory (DFT) methods sometimes struggle
 217 with the correct description and spin state ordering of
 218 transition metal complexes, in particular of manganese
 219 complexes.³⁰ In this work a series of test calculations were
 220 performed with a variety of density functional and ab initio
 221 methods, and the results were compared with experimental
 222 (spectroscopic) data. It should be noted that computational
 223 methods that better reproduce experimental crystal structure
 224 coordinates are often not the preferred methods for
 225 reproducing reaction rates, as found previously.³¹ 226

227 We undertook an extensive benchmarking study of the
 228 $[\text{Mn}(\text{O})(\text{H}_8\text{Cz})(\text{CN})]^-$ complex using a range of density
 229 functional and ab initio methods, particularly aimed at
 230 establishing the amount of Hartree-Fock exchange interaction
 231 needed in the calculations.

232 Optimized geometries were compared against the reported
 233 structural parameters from X-ray absorption spectroscopy
 234 (XAS) published previously^{14a} and calculated using a variety
 235 of density functional methods. An overview of the full account
 236 of the results is given in the Supporting Information (Tables
 237 S1–S4). In general, the results lead to the conclusion that the
 238 BLYP and TPSS density functional methods perform
 239 consistently better than alternative pure density functional
 240 methods for matching the metrical parameters obtained from
 241 XAS (Table S1, Supporting Information). TPSS performed
 242 slightly better than BLYP, as expected according to the Jacob's
 243 ladder scheme.³² Among all three hybrid density functional
 244 methods, B3LYP performed the best except in Medium 244

Table 1. Calculated Adiabatic Singlet-Triplet Energy Gaps (ΔE_{ST}) and Unpaired Spin Density in the Triplet Spin State of $[\text{Mn}(\text{O})(\text{H}_8\text{Cz})(\text{CN})]^-$ Using a Range of Density Functional Methods and Basis Set BS2 on Different Optimized Geometries^{a,b}

geometry	BP86	BLYP	PBE	TPSS	B3LYP	PBE0	TPSSh
BLYP ^c	9.15 (2.13)	9.48 (2.08)	9.14 (2.12)	8.78 (2.11)	1.84 (3.05)	-3.87 (3.44)	5.25 (2.62)
TPSS ^d	9.23 (2.12)	9.41 (2.06)	9.21 (2.11)	8.83 (2.10)	2.15 (3.03)	-3.26 (3.43)	5.47 (2.63)
B3LYP ^e	15.37 (2.77)	14.45 (2.55)	15.48 (2.69)	13.58 (3.07)	0.69 (3.79)	-6.51 (3.99)	6.74 (3.64)

^aRelative energies in kcal mol⁻¹; a positive value denotes a singlet spin ground state. ^bTotal unpaired spin density is given in parentheses as the sum of the absolute values of Mn and O. ^cCalculated Mn–O distances of 1.59 (singlet) and 1.66 (triplet) Å. ^dCalculated Mn–O distances of 1.58 (singlet) and 1.66 (triplet) Å. ^eCalculated Mn–O distances of 1.55 (singlet) and 1.78 (triplet) Å.

245 Absolute Deviation. It is surprising that B3LYP performs better
246 than TPSSh for two reasons: (1) B3LYP contains a larger
247 amount of HF exchange and (2) has a better parametrized
248 correlation functional. On the basis of these results, therefore,
249 we continued the studies with hybrid density functional
250 methods only. The effective core potential-all electron basis
251 set combination SDD/6-31G(d) excelled compared to the
252 other two combinations tested in agreement with previous
253 findings.³³

254 **Spin State Ordering and Electronic Ground State of**
255 **$[\text{Mn}(\text{O})(\text{H}_8\text{Cz})(\text{CN})]^-$.** It is sometimes difficult to calculate
256 excited states and spin state ordering by DFT, because it is
257 formally a ground-state theory. As a consequence, different
258 density functional methods can give inconsistent results,
259 especially for transition metal complexes where near-degeneracy
260 of the d orbitals poses a difficulty for this single-
261 determinant theory.³⁰ The exchange-correlation term is differ-
262 ent for each density functional method, and its value
263 determines the energy associated with electron pairing.
264 Therefore, the correct choice of DFT method influences the
265 obtained results and is extremely important in determining spin
266 state ordering, where many close-lying spin states are present.
267 Indeed, Shaik and co-workers previously demonstrated that
268 the spin state ordering of $[\text{Mn}(\text{O})(\text{H}_8\text{Cz})]$ could vary greatly
269 with different exchange-correlation potentials and/or the
270 amount of HF exchange included.¹³ They also suggested that
271 the spin ground state of $[\text{Mn}(\text{O})(\text{H}_8\text{Cz})(\text{CN})]^-$ should be the
272 triplet spin state as opposed to the experimentally determined
273 singlet spin state of the parent five-coordinate complex. To
274 highlight the spin accessibility and the electronic possibilities of
275 the $[\text{Mn}(\text{O})(\text{H}_8\text{Cz})(\text{CN})]^-$ reactant complex, we show high-
276 lying occupied and low-lying virtual orbitals in **Scheme 2**.

277 The metal orbitals form bonding and antibonding combina-
278 tions with orbitals on the first coordination sphere ligands. In
279 the *xy* plane, the $3d_{x^2-y^2}$ orbital on Mn mixes with $2p\sigma$ orbitals
280 on the nitrogen atoms of the corrolazine ring to give the $\sigma_{x^2-y^2}/$
281 $\sigma_{x^2-y^2}^*$ pair of orbitals, whereas the nonbonding δ_{xy} orbital lies
282 in between the nitrogen atoms. Along the *z* axis, the $3d_z^2$ orbital
283 on Mn mixes with the $2p\sigma$ orbital of oxygen to form the $\sigma_z^2/$
284 $\sigma_z^2^*$ orbitals, whereas the $3d_{xz}/3d_{yz}$ orbitals form π -type
285 interactions with the $2p_x/2p_y$ orbitals to give the π_{xz}/π_{xz}^* and
286 π_{yz}/π_{yz}^* pair of orbitals. In addition, there are several high-lying
287 π orbitals on the corrolazine ligand, and the *a''* shape is shown
288 in **Scheme 2**. This highly dispersed orbital shows similarity to
289 the a_{1u} orbital in heme structures.³⁴ The experimental evidence
290 indicates a closed-shell singlet ground state ($^1A_{LS}$) for
291 manganese(V)–oxo corrolazine complexes. However, the *a''*
292 orbital can become singly occupied through valence tautomer-
293 ism upon binding of a Lewis acid such as Zn^{2+} to the oxo
294 ligand, stabilizing a $^3A''$ electronic state.³⁵ These findings
295 suggest that the orbital manifold is close in energy and various

ground states could be accessible dependent on the local
environmental conditions.

In the closed-shell singlet spin state ($^1A_{LS}$) these sets of
orbitals are occupied as $[\text{core}] \pi_{yz}^2 \delta_{xy}^2$ with $[\text{core}] =$
 $\sigma_{x^2-y^2}^2 \sigma_z^2 \pi_{xz}^2$, and all orbitals are in a low-spin (LS)
configuration. The triplet spin state that retains the +5
oxidation state on Mn has occupation $[\text{core}] \pi_{yz}^2 \delta_{xy}^1 \pi_{xz}^1$
($^3\Pi_{LS}$) and can be described as a high-spin Mn^V species. The
alternative triplet spin state with four unpaired electrons (in
high-spin configuration, $^3\Pi_{HS}$) is different, arising from
promotion of an electron from π_{yz} to π_{yz}^* , and can be
described as high-spin Mn^{IV} antiferromagnetically coupled with
an oxyl radical ($\text{Mn}^{IV}=\text{O}^{\bullet}$).

As the three electronic states ($^1A_{LS}$, $^3\Pi_{LS}$, and $^3\Pi_{HS}$) of
 $[\text{Mn}(\text{O})(\text{H}_8\text{Cz})(\text{CN})]^-$ are expected to be close in energy we
decided to investigate their spin state ordering and relative
energies using various computational models. Although we
attempted to characterize the $^3A''$ as well, which would
represent an Mn^{IV} π -cation–radical configuration, it was not
low enough in energy for any of the systems examined to play a
key role in reactivity. The results obtained for the DFT
methods are summarized in **Table 1**, while raw data can be
found in Tables S1–S5 (**Supporting Information**). Thus, the
 $[\text{Mn}(\text{O})(\text{H}_8\text{Cz})(\text{CN})]^-$ complex was optimized in the singlet
and triplet spin states using BLYP, TPSS, and B3LYP methods.
The pure density functionals (BLYP and TPSS) give almost
identical geometries with a short Mn–O distance below 1.6 Å
in the singlet spin state that implicates a Mn–O triple bond. By
contrast, due to additional antibonding character through
occupation of the π_{xz}^* orbital in the triplet spin state the Mn–
O distance is elongated to 1.66 Å. At the B3LYP level of theory,
the singlet spin state has a somewhat shorter Mn–O distance of
1.55 Å in the singlet spin state but a considerably larger one in
the triplet spin state of 1.78 Å. The group spin densities and
orbital occupations, however, show that the B3LYP optimiza-
tion led to the $^3\Pi_{HS}$ state, whereas the pure density functionals
gave the $^3\Pi_{LS}$ state instead. As a consequence of occupation of
an extra π^* orbital in the $^3\Pi_{HS}$ state the Mn–O distances are
significantly elongated as compared those in the $^3\Pi_{LS}$ state. In
principle, the $^3\Pi_{HS}$ state has two singly occupied π^* orbitals for
the MnO interaction, which would result in significant oxyl
radical character. By contrast, in the $^3\Pi_{LS}$ state only one π^*
orbital is singly occupied and the oxyl character will be
significantly less than in the $^3\Pi_{HS}$ state.

In order to obtain an accurate value of the singlet–triplet
energy gap and the nature of the lowest triplet spin
configuration, we decided to study this chemical system with
a method that allows accurate description of multiconfigura-
tional systems, namely, the complete active space self-consistent
field (CASSCF) method followed by the N-electron valence
state second-order perturbation theory (NEVPT2) that
accounts for dynamic correlation. The CASSCF calculations

utilized either an active space of eight electrons in seven molecular orbitals or 12 electrons in 11 molecular orbitals, i.e., CAS(8,7) or CAS(12,11). The smallest CAS space contained the three oxygen 2p orbitals and four manganese 3d orbitals ($3d_{xz}$, $3d_{yz}$, $3d_{x^2-y^2}$, and $3d_{z^2}$), whereas the larger CAS space included also the HOMO-1, HOMO, LUMO, and LUMO+1 orbitals on the H_8Cz moiety. Due to the size of the chemical system, we were unable to do a geometry optimization at the NEVPT2:CAS level of theory and consequently ran single points on DFT-optimized geometries (either B3LYP or BLYP) only.

Table 2 gives NEVPT2:CAS calculated singlet-triplet energy splitting as well as the unpaired spin population from CASSCF

Table 2. Spin State Energies between the Singlet and Triplet States of $[Mn(O)(H_8Cz)(CN)]^-$ As Calculated with NEVPT2:CAS/B3LYP on Optimized DFT Geometries^b

active space	geometry ^a	ΔE_{ST}	$\rho(Mn)$	$\rho(O)$
(8,7)	BLYP	8.0	2.17	-0.21
(12,11)	BLYP	8.1	2.17	-0.20
(8,7)	B3LYP	9.9	2.40	-0.44
(12,11)	B3LYP	8.8	2.40	-0.43

^aSinglet spin geometries have $r_{MnO} = 1.59$ Å for BLYP and 1.55 Å for B3LYP, and triplet spin geometries use $r_{MnO} = 1.66$ Å for BLYP and 1.78 Å for B3LYP. ^bAlso given are unpaired spin densities on Mn and O.

on the MnO group. In agreement with the DFT results (except PBE0) from Table 1, the singlet spin state is the ground state and well lower in energy than the triplet spin state. The result of the larger CAS(12,11) calculation is almost identical to that found for the CAS(8,7), with the triplet spin state about 8 kcal mol⁻¹ higher in energy. Therefore, the high-lying occupied and low-lying virtual corrolazine orbitals had little contribution to the singlet-triplet splitting. In addition, the radical character in the triplet spin states implicates a situation closest to the $^3\Pi_{LS}$ state with two unpaired electrons in δ_{xy} and π^*_{xz} (see the natural orbitals and their corresponding occupancies in the Supporting Information Tables S19 and S20 and Figures S2-S9) as also found for pure density functional methods.

By contrast, using the B3LYP-optimized geometry a mixed state in between the $^3\Pi_{LS}$ and the $^3\Pi_{HS}$ configurations is obtained with spin density of about 2.4 on Mn and -0.4 on O. As such, the $^3\Pi_{HS}$ state found by hybrid functionals can be attributed to a lack of electronic correlation of the Hartree-Fock orbitals.

DFT-optimized geometries were used as the input geometry for NEVPT2:CAS single-point energy calculations because the system of interest is too large to be optimized at that level of theory. Both NEVPT2:CAS and pure density functional methods find the singlet spin state of $[Mn(O)(H_8Cz)(CN)]^-$ to be the ground state and use optimized geometries that match the experimentally determined ones by the EXAFS methods excellently.^{14a} However, in order to determine the variation in singlet-triplet energy levels, we did an additional set of calculations on the lowest lying singlet and triplet spin states with variable Mn-O distances. Thus, we performed constrained surface scans using NEVPT2:CAS along the Mn-O bond using B3LYP relaxed geometries. As can be seen from Figure 1, such constraints should give insight into the adiabatic and diabatic spin state ordering with varying Mn-O distance. The singlet spin state stays the ground state as the Mn-O bond

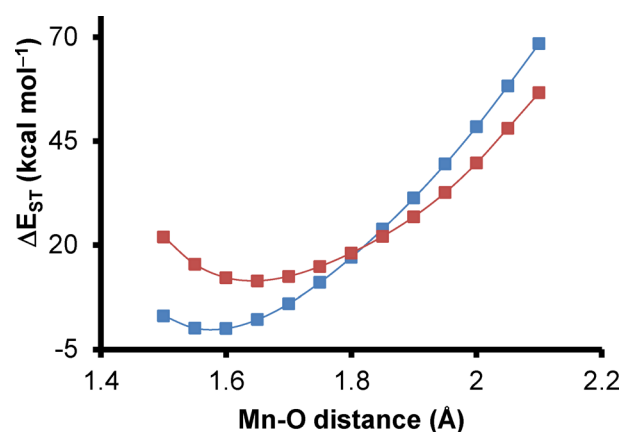


Figure 1. Constrained potential energy scan along the Mn-O bond of $[Mn(O)(H_8Cz)(CN)]^-$ calculated by NEVPT2:CAS(8,7) with B3LYP. Singlet scans are shown in blue solid squares. Triplet scans are shown in red solid squares. Energies are shown relative to the minimum of the singlet complex for clarity.

stretches from 1.50 to 1.75 Å, consistent with the spin state ordering predicted by pure density functional methods as well as B3LYP. At 1.55 Å, the singlet spin state is the ground state and resides at the minimum point of the singlet PES. At 1.65 Å, the singlet spin state is still the ground state while triplet spin state resides at its minimum point of the triplet PES, consistent with the geometries optimized for the singlet and triplet manganese-oxo species. The triplet and singlet spin states become near-degenerate in the range between 1.75 and 1.85 Å with a spin population of ~ 2.4 on Mn and ~ -0.4 on O. This distance is in line with Mn(IV) species reported in the literature³⁵ and is the operating bond length during the transition states (vide infra). The triplet spin state becomes the ground state at 1.9 Å in favor of the singlet spin state by ~ 4 kcal mol⁻¹ with a spin population of 2.5 on Mn and -0.6 on O. At 2.1 Å, the spin population is 2.7 on Mn and -0.8 on O. Therefore, the scan along the Mn-O bond distance confirms that a fully optimized NEVPT2 structure would lie in a low-spin ground state, with a significant singlet-triplet energy gap.

The calculations presented here implicate that multireference techniques including NEVPT2 and CASSCF propose the $[Mn(O)(H_8Cz)(CN)]^-$ system to be in a closed-shell singlet ground state. However, its separation from the nearest triplet spin state is considerably larger than previously thought and of the order of 8-10 kcal mol⁻¹, which is at a thermally inaccessible level at room temperature. In addition, the singlet-triplet transition from $^1A_{LS}$ to $^3\Pi_{HS}$ requires a double electron excitation, one from δ_{xy} to π^* and one from π to π^* . As such, this is a spin-forbidden process and may not proceed with a large probability. Moreover, the spin distribution gives a slightly favorable $^3\Pi_{LS}$ state over alternative triplet spin states. The only exception came from the CASSCF spin distribution calculated on top of B3LYP-optimized geometry, which features an unusually long Mn-O distance at 1.78 Å. However, surface scans along the Mn-O bond by NEVPT2:CAS rule out the B3LYP-optimized geometry residing on the minimum of the triplet potential surface of $^3\Pi_{LS}$. B3LYP optimization very likely converged to the higher excited state, the $^3\Pi_{HS}$, of the triplet state, as evidenced by the corresponding spin populations, owing to the lack of electron correlation from the HF exchange parameters.

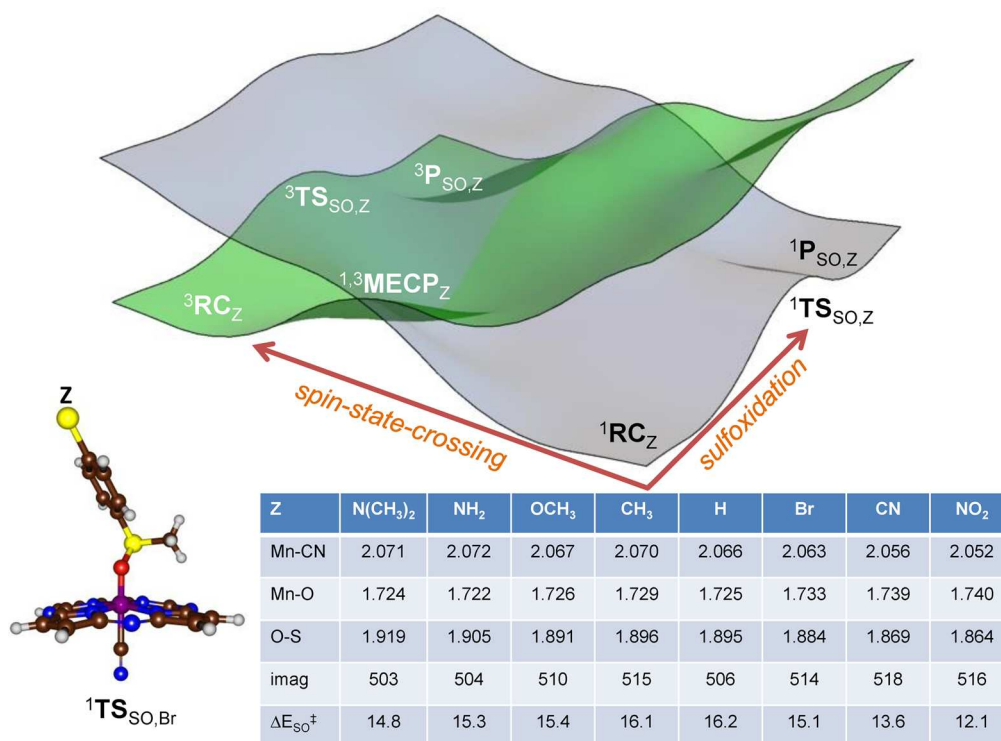


Figure 2. Potential energy landscape for the sulfoxidation of para-*Z*-substituted thioanisole (Sub_Z, Z = N(CH₃)₂, NH₂, OCH₃, CH₃, H, Br, CN, and NO₂) by ^{1,3}[Mn(O)(H₈Cz)(CN)]⁻. Table gives relative energies (ΔE_{SO}) for ¹TS_{SO} as calculated with basis set BS2 and given in kcal mol⁻¹. Optimized geometries of ¹TS_{SO} give bond lengths in Angstroms and the imaginary frequency of the transition state in cm⁻¹. Data calculated at RIJCOSX-TPSSH-D3/def2-QZVPP/ZORA//RIJCOSX-B3LYP-D3/SDD/6-31G(d) in Orca. RC is the reactant complex, TS_{SO} is the sulfoxidation transition state, P_{SO} is the sulfoxide product complex, and MECP refers to the minimum energy crossing point between the singlet and the triplet spin state.

437 The pure density functional methods better reproduce the
 438 singlet–triplet energy gap found by NEVPT2:CAS compared
 439 to the hybrid methods. The spin populations found by
 440 NEVPT2:CAS are reproduced well with a BLYP single point
 441 on a geometry optimized with a hybrid density functional
 442 method. We, therefore, studied the sulfoxidation of para-*Z*-
 443 substituted thioanisoles mediated by [Mn(O)(H₈Cz)(CN)]⁻ at
 444 different spin states by BLYP and TPSSH on B3LYP-optimized
 445 geometries. B3LYP is used for geometry optimizations for its
 446 success in reproducing experimental rate constants in the
 447 literature.³⁶ TPSSH is also used for reaction energetics for the
 448 fact that it is the only hybrid functional that matches the spin
 449 state ordering found by NEVPT2:CAS and is the highest rank
 450 on the Jacob’s ladder scheme among the functionals tested in
 451 the section above. As such, the procedure that is used in the
 452 following represents a geometry optimization at the B3LYP
 453 level of theory followed by a single-point calculation using
 454 BLYP or TPSSH to obtain more reliable spin state energetics.

455 **Calculated Hammett Plots for the Reaction of**
 456 **[Mn(O)(H₈Cz)(CN)]⁻ with Thioanisole Derivatives.** In
 457 previous work, our groups have shown that [Mn(O)(H₈Cz)-
 458 (CN)]⁻ reacts with para-*Z*-substituted thioanisoles efficien-
 459 tly.^{14a} The experimentally determined plot of the logarithms of
 460 the rate constants of para-*Z*-substituted versus para-H-
 461 substituted thioanisole reactions, i.e., log(k_Z/k_H), did not give
 462 a linear correlation with the Hammett constant (σ_p) of the
 463 substituent but rather a “V-shaped” Hammett correlation,
 464 Scheme 1. It was proposed that different reaction mechanisms
 465 were operative, depending on the nature of the substituent. In
 466 particular, it was suggested that a nucleophilic attack on the

metal–oxo group took place with substrates with electron- 467
 donating substituents to give a negative Hammett slope, 468
 whereas an electrophilic attack occurred with substrates with 469
 electron-withdrawing substituents instead.^{14a} Interestingly, the 470
 axially vacant five-coordinated [Mn^V(O)(Cz)] species did not 471
 react with any of the para-*Z*-substituted thioanisoles within a 472
 measurable time, and hence, a considerable rate enhancement is 473
 observed upon binding of the axial ligand.^{14b} Our work as well 474
 as that of Fujii and co-workers³⁷ showed computationally that 475
 such a drastic rate enhancement tracked with the increased 476
 stability of the product Mn(III) complex, and this thermody- 477
 namic driving force extended into the transition state through 478
 the Bell–Evans–Polanyi principle. Clearly, a nonlinear 479
 Hammett plot would correspond to a change in reaction 480
 mechanism between substrates with electron-donating and 481
 electron-withdrawing para substituents. We calculated the 482
 substrate sulfoxidation of para-*Z*-substituted-thioanisole (Z = 483
 N(CH₃)₂, NH₂, OCH₃, CH₃, H, Br, CN, and NO₂) with 484
^{1,3}[Mn(O)(H₈Cz)(CN)]⁻. Figure 2 displays the calculated 485
 potential energy profiles for substrate sulfoxidation by ^{1,3}[Mn- 486
 (O)(H₈Cz)(CN)]⁻, with structural and energetic values for all 487
¹TS_{SO,Z} geometries. The singlet spin barriers range from 12.1 to 488
 16.2 kcal mol⁻¹ for the substrates studied here. All data for the 489
 other intermediates, transition states, and products can be 490
 found in the Supporting Information (Tables S7–S13). The 491
 sulfoxidation reaction is concerted via a single oxygen insertion 492
 transition state TS_{SO} from a reactant complex (RC) and leading 493
 to products P_{SO}. These labels are given the subscript for the Z 494
 substituent for the para-*Z*-substituted thioanisole substrate 495
 used. The mechanism follows previously reported substrate 496

497 sulfoxidation reactions by analogous chemical systems.³⁸ In all
 498 cases, the isolated reactants and reactant complexes are in a
 499 closed-shell singlet ground state, and as such the spin state
 500 ordering does not change upon the formation of an oxidant–
 501 substrate complex RC. However, $^1\text{TS}_{\text{SO,Z}}$ is found to be higher
 502 in energy than $^3\text{TS}_{\text{SO,Z}}$ in all cases and so is the ordering of the
 503 product complexes. To confirm the spin state ordering and find
 504 the energy splitting of the two transition states, we ran
 505 NEVPT2:CAS(8,7) single point on the optimized geometries
 506 of $^{1,3}\text{TS}_{\text{SO,NO}_2}$. These calculations establish that the triplet spin
 507 barrier is 4.3 kcal mol⁻¹ lower in energy than the singlet spin
 508 state. Furthermore, at the NEVPT2:CAS(8,7) level of theory
 509 $^3\text{TS}_{\text{SO,CH}_3}$ had a barrier of 11.8 kcal mol⁻¹ relative to the
 510 reactant complex, which is not dramatically different from the
 511 values obtained at RIJCOSX-TPSSH-D3/def2-QZVPP/
 512 ZORA//RIJCOSX-B3LYP-D3/SDD/6-31G(d). As such, the
 513 barrier heights displayed in Figure 2 match the NEVPT2:CAS-
 514 (8,7) and experimental values well. Moreover, the high-level
 515 NEVPT2:CAS(8,7) calculations implicate a much smaller
 516 singlet–triplet energy gap in the transition states as initially
 517 thought, whereas the gap is considerable in the reactant
 518 complexes.

519 The potential energy landscape covering the two spin states
 520 for substrate sulfoxidation by $[\text{Mn}(\text{O})(\text{H}_8\text{Cz})(\text{CN})]^-$ is
 521 schematically depicted at the top of Figure 2. This mechanism
 522 is the same for all substrates investigated here. Thus, there is a
 523 substrate sulfoxidation mechanism from isolated reactants via
 524 RC and TS_{SO} leading to products on the singlet spin state (gray
 525 surface), and there is an analogous pathway on the triplet spin
 526 state (green surface). A 3D representation of the potential
 527 energy surface is shown in Figure 2, where the two surfaces are
 528 bisected on a spin crossing line, with the lowest energy crossing
 529 point the minimum energy crossing point (MECP). The spin
 530 transition from singlet to triplet is located on the axis to the left.
 531 Thus, the spin crossing seam will have a MECP, where the
 532 singlet and triplet energies overlap. As such the landscape will
 533 follow a bifurcation pathway, whereby one pathway from singlet
 534 spin reactants will directly lead to sulfoxide products via $^1\text{TS}_{\text{SO}}$,
 535 whereas the alternative pathway will proceed via a spin
 536 crossover via $^{1,3}\text{MECP}$ to the triplet spin state surface followed
 537 by sulfoxidation through $^3\text{TS}_{\text{SO}}$ en route to products.

538 To find out whether the singlet and triplet spin state surfaces
 539 cross and could lead to a spin state change along the reaction
 540 mechanism, we calculated minimum energy crossing points
 541 (MECP) for the singlet to triplet transitions using the
 542 procedures of Harvey.³⁹ Thus, our MECP-calculated singlet–
 543 triplet crossing points give chemical structures (see Figure 3)
 544 that do not lie on the substrate sulfoxidation reaction pathway.

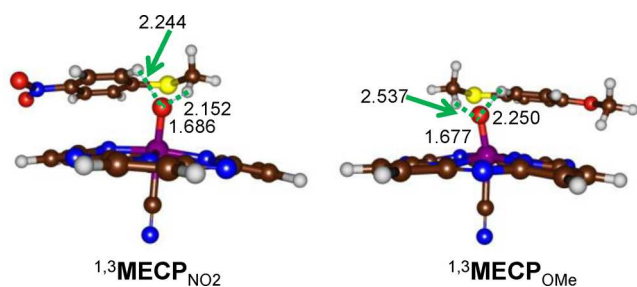


Figure 3. MECP-optimized geometries for the singlet–triplet transition for $[\text{Mn}(\text{O})(\text{H}_8\text{Cz})(\text{CN})]^-$ with *p*-NO₂-thioanisole and *p*-OCH₃-thioanisole. Bond lengths are given in Angstroms.

In particular, the sulfur atom of the substrate is oriented away
 545 from the terminal oxo ligand, and there is no S–O bond
 546 formation. Instead, the MECP structures show a weak
 547 (hydrogen bonding) interaction between substrate and oxidant
 548 with the protons of the methyl and phenyl groups of the
 549 substrate forming nonbonding interactions with the oxo ligand.
 550 The singlet–triplet crossing does not appear to happen along
 551 the sulfoxidation mechanism but rather occurs as a spin state
 552 crossover in the reactant complexes.

The $^{1,3}\text{MECP}$ structures have long Mn–O distances of well
 554 over 1.67 Å and resemble the triplet spin reactants. Our MECP-
 555 calculated crossing points are approximately 4–5 kcal mol⁻¹
 556 higher in energy than $^1\text{RC}_Z$ and correspond to a triplet spin
 557 state with about two unpaired electrons on the MnO unit.
 558 Recall that in the reactant structures a singlet–triplet energy
 559 gap of 8 kcal mol⁻¹ was obtained using the highest level of
 560 theory, and, hence the real crossing points may be well higher
 561 than that. Therefore, upon elongation of the Mn–O bond
 562 similarly to the scan in Figure 1, the surface crossing is reached.
 563 These MECP structures can lead to a singlet–triplet crossing
 564 during the lifetime of the reactant complexes but may not
 565 connect to the sulfoxide products and/or transition states. In
 566 the event of long-lived reactant complexes a thermal Boltzmann
 567 equilibration may populate the triplet spin state and lead to
 568 reactivity with sulfides on the lower energy surface. However,
 569 based on the energetic separation by the singlet and triplet spin
 570 state as calculated with NEVPT2:CAS, we expect the thermal
 571 occupation of the triplet spin state to be very small.

Key bond lengths of the optimized low-spin transition state
 573 structures $^1\text{TS}_{\text{SO,Z}}$ are given in Figure 2. As follows for the series
 574 $Z = \text{N}(\text{CH}_3)_2$ to $Z = \text{NO}_2$ the Mn–CN distance gradually
 575 decreases from 2.071 to 2.052 Å, while the Mn–O distance
 576 elongates from 1.724 to 1.740 Å in an almost linear fashion. At
 577 the same time the O–S distance decreases from $Z = \text{N}(\text{CH}_3)_2$
 578 to $Z = \text{NO}_2$ from 1.919 to 1.864 Å. These trends imply that an
 579 electron-withdrawing substituent, such as NO₂, gives transition
 580 states with structures that are later on the potential energy
 581 surface (shorter S–O bonds) than substrates with electron-
 582 donating substituents, in agreement with what was observed
 583 previously on analogous systems.⁴⁰ All transition states are
 584 characterized with a single imaginary mode for the S–O bond
 585 formation with values in the range of $i503$ – $i518$ cm⁻¹.

The Hammett correlation for the enthalpy of activation of
 587 para-*Z*-substituted thioanisole in reaction with $[\text{Mn}(\text{O})-$
 588 $(\text{H}_8\text{Cz})(\text{CN})]^-$ versus σ_p for the singlet and triplet spin
 589 sulfoxidation barriers is shown in Figure 4. The values of
 590 $\log(k_Z/k_H)$ were estimated from the enthalpies of activation,
 591 see Supporting Information for details. The computations
 592 reproduce experiment well for the singlet spin state only, giving a
 593 “V-shaped” Hammett plot, regardless of the choice of
 594 functionals and basis sets, although the calculations give a
 595 slightly earlier mechanistic switch from $Z = \text{Br}$ to $Z = \text{H}$ with
 596 respect to experiment. In particular, the triplet spin barriers give
 597 a linear correlation between the Hammett σ_p value and $\log k_Z/$
 598 k_H for the full set of substrates tested in the range from $\sigma_p =$
 599 -0.83 ($Z = \text{N}(\text{CH}_3)_2$) to $\sigma_p = +0.778$ (NO₂). Clearly, the
 600 experimentally determined V-shaped Hammett plot cannot
 601 correspond to rate constants obtained through the triplet spin
 602 pathway. These results also imply that the spin state crossing
 603 from triplet to singlet before the rate-determining step is
 604 unlikely, in line with the conclusion reached from the low
 605 spin–orbit coupling constants.

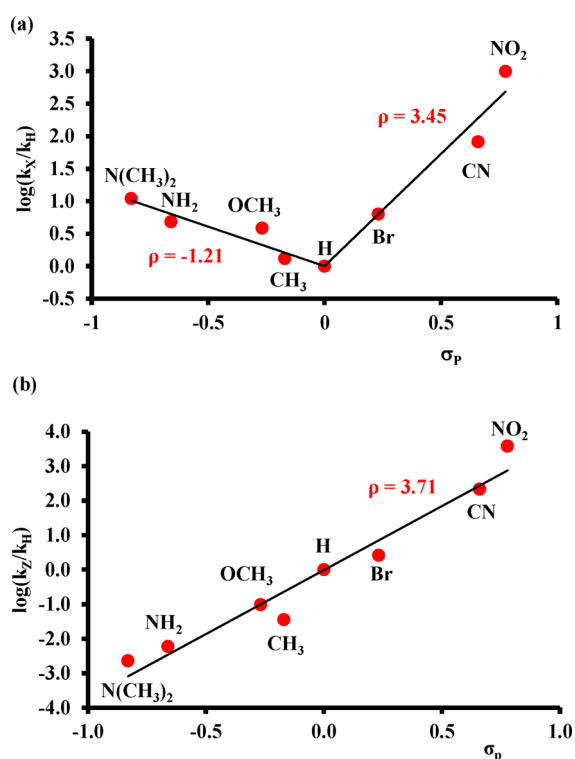


Figure 4. Computational Hammett plot for the reaction of singlet and triplet $[\text{Mn}(\text{O})(\text{H}_8\text{Cz})(\text{CN})]^-$ with para-*Z*-substituted thioanisole derivatives. Data calculated at RIJCOSX-TPSSH-D3/def2-QZVPP/ZORA//RIJCOSX-B3LYP-D3/SDD/6-31G(d) and includes zero-point, thermal, and solvent corrections. (a) Correlation for singlet spin barriers (${}^1\text{TS}_{\text{So,Z}}$). (b) Correlation for triplet spin barriers (${}^3\text{TS}_{\text{So,Z}}$).

As computational trends often give a systematic error with respect to experiment as shown before, they do tend to correctly reproduce regio- and chemoselectivities of reaction as well as product isotope effects.⁴¹ In particular, the computation gives a somewhat wider energy gap between the enthalpy of activation of the para-*Z* substituted thioanisoles with respect to the experimental trends. As a consequence, the Hammett ρ values are larger than those reported in ref 14a. The deviation between experimental and computational rate constants may have to do with the incorrect description of solvent and neglecting entropic and thermal corrections in the calculations.

Technically, the transition state can also exist in a triplet and quintet spin state, and therefore, we calculated the trends for sulfoxidation reactions on those spin states and show the results in Figures 4b and S1. The calculated relative energies from DFT for the triplet and quintet spin states give a good match to those obtained from the NEVPT2:CAS(12,11) calculations. However, despite the fact that the triplet and quintet barriers have structural similarities to the singlet spin state transition states, no mechanistic switch was observed when the rate constant ratio $\log(k_Z/k_H)$ was plotted against the Hammett parameter. For the full set of substrates, a linear trend with positive slope was found. The calculated Hammett plots for the triplet and quintet spin states do not match with experiment, indicating that these barriers cannot be the rate-determining step in the reaction mechanism. These findings also suggest that the spin-orbit coupling for the singlet-triplet transition is small, and little or no conversion from singlet to triplet takes

place during the lifetime of the reactant complexes. We conclude that the reaction most likely takes place on a dominant singlet spin state surface. There is a spin state crossing to a more stable spin state only after passing the transition state, and this crossing then happens through thermal equilibrium of product complexes, forming a final quintet spin Mn(III) product as experimentally observed.^{12,13} To confirm these results, the spin-orbit coupling (SOC) constants for all systems were calculated (Table 3). Values ranging from 2.9

Table 3. Spin-Orbit Coupling at the Triplet Transition States of Sulfoxidation of Different Para-*Z*-Substituted Thioanisoles by $[\text{Mn}(\text{O})(\text{H}_8\text{Cz})(\text{CN})]^-$ (values in cm^{-1})

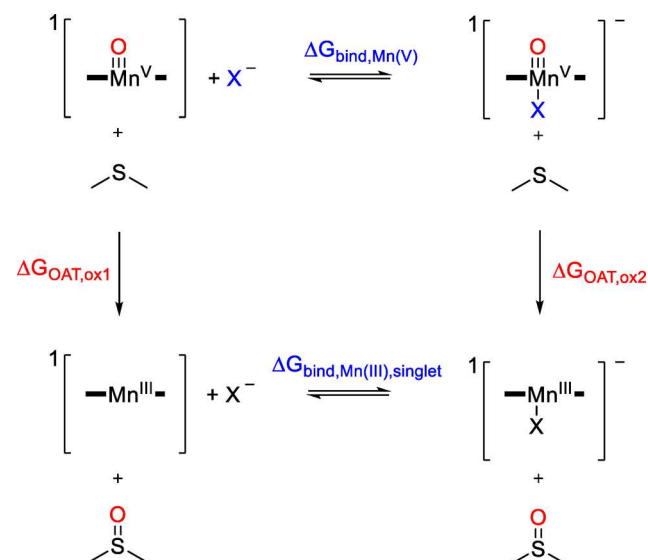
Z	OCH ₃	CH ₃	H	Br	CN	NO ₂
SOC	2.9	3.3	3.7	5.0	3.9	3.6

cm^{-1} for *p*-OCH₃-thioanisole to 5.0 cm^{-1} for *p*-Br-thioanisole are found. These SOC values are very small and implicate little or no spin state change, and the highest probability will lie on the low-spin surface. These give further support for single-state reactivity on the low-spin state.

As shown above, the substrate sulfoxidation reaction by manganese(V)-oxo corrolazine complexes is dependent on the axial ligand bound to the manganese center and on the para-*Z*-substituent of the thioanisole substrate. In the following we will analyze the properties associated with these trends in detail.

Nature of the Axial Ligand on Reactivity Patterns. Similarly to studies on manganese(V)-oxo corrolazine complexes reported previously^{12,14} as well as heme and nonheme iron systems,^{43,44} the axial ligand can affect the reactivity properties of metal-oxo complexes dramatically. In particular, an electron-donating or electron-withdrawing axial ligand can influence the electron affinity of the oxidant and/or the $\text{p}K_a$ of the oxo group and thereby affect the reactivity patterns and regioselectivity distributions as seen before, for instance, in P450 chemistry.⁴⁵ In order to generalize and understand the axial ligand effects we set up a thermochemical cycle as shown in Scheme 3.

Scheme 3. Thermochemical Reaction Scheme Highlighting Ligand Binding versus Oxygen-Atom Transfer



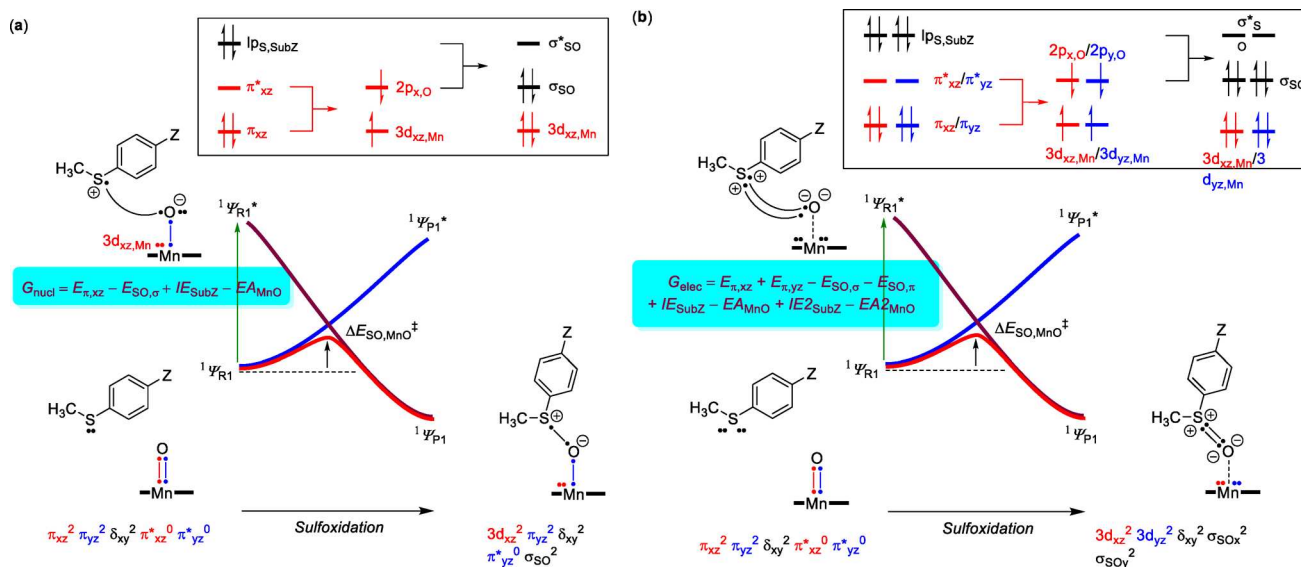


Figure 5. VB curve crossing diagram for nucleophilic and electrophilic sulfoxidation reactions. For explanations see text.

667 The top reaction in Scheme 3 represents the binding
 668 equilibrium of an axial ligand to the manganese(V)–oxo
 669 corrolazine with free energy difference $\Delta G_{\text{bind,Mn(V)}}$. The
 670 bottom reaction, by contrast, represents the binding equi-
 671 librium of an axial ligand to a singlet spin manganese(III)
 672 corrolazine complex with free energy difference $\Delta G_{\text{bind,Mn(III)}}$.
 673 The oxygen-atom transfer (OAT) reaction on the singlet spin
 674 state will lead to singlet spin manganese(III) products.
 675 However, the singlet spin manganese(III) products can through
 676 thermal collisions convert to the more stable quintet spin
 677 products afterward. The two vertical reactions in Scheme 3
 678 describe the OAT reactions of thioanisole with $[\text{Mn}^{\text{V}}(\text{O})-$
 679 $(\text{H}_8\text{Cz})]$ (left) and $[\text{Mn}^{\text{V}}(\text{O})(\text{H}_8\text{Cz})\text{X}]^-$ (right), which have an
 680 overall driving force of $\Delta G_{\text{OAT,ox1}}$ and $\Delta G_{\text{OAT,ox2}}$, respectively.
 681 Thus, for the Born cycle in Scheme 3, the sum of the four free
 682 energy values will be zero, eq 1.

$$\Delta G_{\text{bind,Mn(V)}} + \Delta G_{\text{OAT,ox2}} - \Delta G_{\text{bind,Mn(III)}} - \Delta G_{\text{OAT,ox1}} = 0 \quad (1)$$

684 Therefore, the change in binding strength of an axial ligand
 685 to a manganese(V)–oxo versus a manganese(III) center will be
 686 equal to the free energy change of sulfoxidation between the
 687 axially ligated and the nonaxially ligated complexes, eq 2.

$$\Delta G_{\text{bind,Mn(V)}} - \Delta G_{\text{bind,Mn(III)}} = \Delta G_{\text{OAT,ox1}} - \Delta G_{\text{OAT,ox2}} \quad (2)$$

689 If we assume that the driving force change between
 690 $[\text{Mn}(\text{O})(\text{H}_8\text{Cz})]$ and $[\text{Mn}(\text{O})(\text{H}_8\text{Cz})\text{X}]^-$ is proportional to
 691 the free energy of activation change then based on transition
 692 state theory we can replace the OAT driving forces with the
 693 reaction rates for the oxidation reactions and essentially the rate
 694 enhancement $k_{\text{ox1}}/k_{\text{ox2}}$. The correlation between axial ligand
 695 binding strength and rate enhancement with R being the gas
 696 constant and T the actual temperature is given in eq 3.
 697 Consequently, the stronger the binding strength difference
 698 between the four-coordinate manganese(III) and five-coor-
 699 dinate manganese(V)–oxo complex, the stronger will be the
 700 rate enhancement for substrate activation. This conclusion was
 701 observed and reported by Fujii earlier.⁴⁶

$$\Delta G_{\text{bind,Mn(V)}} - \Delta G_{\text{bind,Mn(III)}} \propto RT \ln k_{\text{ox2}}/k_{\text{ox1}} \quad (3) \quad 702$$

In order to test our hypothesis, we calculated the binding
 703 strength of axial ligands to manganese(III) and manganese-
 704 (V)–oxo corrolazine. With $\text{X} = \text{CN}^-$, we calculated an axial
 705 ligand bond strength difference between the manganese(V)–
 706 oxo and the manganese(III) complexes of $\Delta G_{\text{bind,Mn(V)}} -$
 707 $\Delta G_{\text{bind,Mn(III)}} = 48.4 \text{ kcal mol}^{-1}$. If we assume a correlation
 708 factor of 1.6 for eq 3 based on Marcus theory,⁴⁷ this would
 709 correspond with a rate enhancement $k_{\text{ox2}}/k_{\text{ox1}}$ of 4×10^7 for
 710 oxygen-atom transfer. Indeed, no reactivity was observed for
 711 thioanisoles with $[\text{Mn}(\text{O})(\text{H}_8\text{Cz})]$ in agreement with a
 712 considerably slower reaction rate as compared to the
 713 $[\text{Mn}(\text{O})(\text{H}_8\text{Cz})(\text{CN})]^-$ system.^{14a} We further attempted to
 714 predict the rate enhancement of alternative complexes with $\text{X} =$
 715 F^- , N_3^- , OCN^- , and NO_3^- , see Supporting Information
 716 (Tables S23 and S24). We find similar rate enhancements of
 717 $[\text{Mn}(\text{O})(\text{H}_8\text{Cz})\text{X}]$ with $\text{X} = \text{CN}^-/\text{F}^-$ in agreement with
 718 experimental rate enhancements measured for dehydroanthra-
 719 cene dehydrogenation by $[\text{Mn}(\text{O})(\text{H}_8\text{Cz})\text{X}]^-$.¹² The studies
 720 also show that much lower rate enhancements may be expected
 721 for manganese(V)–oxo corrolazine complexes with N_3^- ,
 722 OCN^- , and NO_3^- ligands, since these are much weaker
 723 bound ligands. In particular, an N_3^- , OCN^- , or NO_3^- ligand
 724 binds much weaker to the Mn^{III} complex, and therefore, their
 725 rate enhancements are not as dramatic as with F^- and CN^- that
 726 see major differences in the binding strength between the Mn^{III}
 727 and the $\text{Mn}^{\text{V}}(\text{O})$ complexes.
 728

Valence Bond Modeling of Reactivity Patterns.

729 Previously, we used valence bond curve-crossing diagrams
 730 extensively to rationalize reactivity patterns of iron(IV)–oxo
 731 oxidants with substrates.⁴⁸ These studies explained why the
 732 reactions were stepwise but also pinned down the electro-
 733 chemical and thermochemical properties of oxidant and
 734 substrate that drive the reaction. The VB curve-crossing
 735 diagrams give a rationalization of the electronic changes to
 736 oxidant and substrate during the oxygen-atom transfer process.
 737 Figure 5 gives the two VB diagrams representing the
 738 nucleophilic and electrophilic reaction pathways for thioanisole
 739 sulfoxidation by $[\text{Mn}^{\text{V}}(\text{O})(\text{H}_8\text{Cz})(\text{CN})]^-$.
 740

741 The landscapes start on the bottom-left with the reactant
 742 complexes, which are manganese(V)–oxo complexes in the
 743 closed-shell singlet spin state ($^1A_{1S}$) with orbital occupation
 744 [core] $\pi_{yz}^2 \delta_{xy}^2 a''^2$. Key bonds in the VB structures are indicated
 745 with two dots separated by a line. In particular, along the Mn–
 746 O bond there are interactions due to the π and π^* orbitals for
 747 mixing of the metal $3d_{xz}$ and $3d_{yz}$ atomic orbitals with 2p
 748 orbitals on the oxo group. The π_{xz}/π_{xz}^* pair of orbitals is
 749 depicted in red, while the π_{yz}/π_{yz}^* pair of orbitals is given in
 750 blue. The para-Z-substituted thioanisole substrate (SubZ) is
 751 located in the vicinity, and one of the sulfur lone pairs is
 752 highlighted with two dots. Upon oxygen-atom transfer some of
 753 the bonds break and electrons are migrated between groups as
 754 shown in the corresponding VB structures of the two possible
 755 product VB wave functions in part a and b. In VB theory, the
 756 reactant state connects to an excited state in the sulfoxide
 757 product, whereas the product wave function is linked to an
 758 excited state of the reactant wave function. Along the reaction
 759 pathway the two wave functions cross, leading to an avoided
 760 crossing that results in a transition state for the reaction. It has
 761 been shown that the excitation energy (G) from the reactant to
 762 the product state in the geometry of the reactants is
 763 proportional to the barrier height of the reaction, i.e., the
 764 energy difference between $^1\Psi_{R1}$ and $^1\Psi_{R1}^*$ in Figure 5a.
 765 Therefore, we compare VB structures of the ground and excited
 766 state complexes in the geometry of the reactants to ascertain
 767 the properties of oxidant and substrate that determine the
 768 reactivity.

769 We consider two possibilities for the reaction mechanism,
 770 namely, a nucleophilic and an electrophilic pathway. The
 771 nucleophilic pathway is shown in Figure 5a and includes a
 772 single bond formation between the substrate and the oxo
 773 group. In the process, the π_{xz}/π_{xz}^* pair of orbitals along the
 774 Mn–O bond split back into atomic orbitals, i.e., $2p_O$ and
 775 $3d_{xz,Mn}$, both with one electron, which will cost the system an
 776 amount of energy $E\pi_{xz}$. The radical in $2p_O$ forms a bond with
 777 one electron from the lone pair on sulfur, and the S–O bond
 778 formed will have an energy $E_{SO,\sigma}$. The second electron from the
 779 lone pair is transferred to the manganese, so that the excitation
 780 energy for the nucleophilic mechanism (G_{nucl}) essentially
 781 includes the one-electron ionization (IE_{SubZ}) of the substrate
 782 and the one-electron reduction of the oxidant (EA_{MnO}) as
 783 shown by eq 4.

$$784 \quad G_{\text{nucl}} = E_{\pi_{xz}} - E_{SO,\sigma} + IE_{\text{SubZ}} - EA_{\text{MnO}} \quad (4)$$

785 As shown in Figure 5a, the reactant has three sets of bonding
 786 orbitals along the Mn–O bond, namely, the $\sigma_{z2}/\sigma_{z2}^*$, π_{yz}/π_{yz}^*
 787 and π_{xz}/π_{xz}^* pair of orbitals, which formally gives the Mn–O
 788 interaction a triple bond of which we only show the π/π^* pairs
 789 in the figure. However, upon thioanisole attack the triple bond
 790 is converted into a double bond as also seen from the distances
 791 displayed in Figure 1 as compared to the much shorter reactant
 792 Mn–O distances.

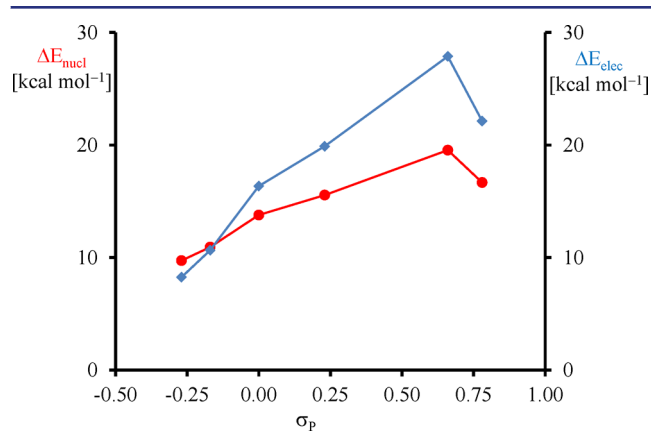
793 The alternative reaction mechanism would provide us an
 794 electrophilic reaction with excitation energy G_{elec} , eq 5. Now
 795 the π_{xz}/π_{xz}^* and π_{yz}/π_{yz}^* pair of orbitals revert back into atomic
 796 orbitals, and both lone pairs of sulfur form a bond with the two
 797 newly generated 2p orbitals on oxygen. In this process the
 798 substrate loses two electrons to the metal, so that the G_{elec} value
 799 will be proportional to twice the substrate ionization energy
 800 plus the first and second reduction energy of the manganese–
 801 oxo complex. Of course the S=O bond formed with energy
 802 $E_{S=O}$ is now a double bond rather than a single bond in the

nucleophilic pathway and is based on the energy to form the σ 803
 bond ($E_{SO,\sigma}$) and the energy to form the π bond ($E_{SO,\pi}$). 804

$$805 \quad G_{\text{elec}} = E_{\pi_{xz}} + E_{\pi_{yz}} - E_{SO,\sigma} - E_{SO,\pi} + IE_{\text{SubZ}} - EA_{\text{MnO}} \\ + IE_{2\text{SubZ}} - EA_{2\text{MnO}} \quad (5)$$

To understand the driving force for the switch of trend in the 806
 Hammett correlation, one can picture two reaction mechanisms 807
 leading to products, namely, those described in Figure 5a and 808
 5b, respectively. Pathway A can be formally described as 809
 oxidation of the oxo group by manganese(V) to form 810
 manganese(IV)–oxyl followed by radical coupling between 811
 the oxyl radical and sulfur radical into an S–O bond. This 812
 pathway will be followed by substrates with electron-with- 813
 drawing substituents such as NO_2 and compensates for the 814
 lower ionization energy of the thioanisole by delaying oxidation 815
 of sulfur until later along the mechanism. 816

To strengthen our hypothesis we evaluated values of G_{nucl} 817
 and G_{elec} for all substrates SubZ using eqs 4 and 5 818
 and subsequently converted those to sulfoxidation barrier heights by 819
 multiplying with a factor of 1/3.⁴⁹ The correlations of these 820
 parameters with the Hammett parameter σ_p are shown in 821
 Figure 6. Thus, we calculated the one-electron ionization 822 823



823 **Figure 6.** VB predicted values of the barrier heights ΔE_{nucl} and ΔE_{elec} 824
 from first principles. Values are in kcal mol⁻¹ and plotted against the 825
 σ_p Hammett parameter. 826

energy of all substrates (IE_{SubZ}) and the one-electron reduction 823
 of $[\text{Mn}(\text{O})(\text{H}_8\text{Cz})(\text{CN})]^-$ (EA_{MnO}). In addition, we evaluated 824
 the one-electron ionization of the oxidized substrates ($IE_{2\text{SubZ}}$) 825
 and the one-electron reduction of $[\text{Mn}(\text{O})(\text{H}_8\text{Cz})(\text{CN})]^{2-}$, 826
 i.e., $EA_{2\text{MnO}}$. 827

Then, we took one-half the energy gap between the π_{xz} and 828
 the π_{xz}^* molecular orbitals in the singlet spin state as a measure 829
 for $E_{\pi_{xz}}$ and utilized the same procedure for $E_{\pi_{yz}}$. Finally, the 830
 strength of the σ and π orbitals along the S–O bond was 831
 estimated from the energy gap between the $\sigma_{SO}/\sigma_{SO}^*$ and the 832
 π_{SO}/π_{SO}^* orbitals from the individual isolated product 833
 structures. The resulting values of G_{nucl} and G_{elec} for each 834
 reaction of $[\text{Mn}(\text{O})(\text{H}_8\text{Cz})(\text{CN})]^-$ with substrate SubZ (Z = 835
 OCH_3 , CH_3 , H, Br, CN, and NO_2) were calculated and 836
 converted into barrier heights and plotted versus the Hammett 837
 parameter σ_p of the substrate. As can be seen from Figure 6, the 838
 value for ΔE_{nucl} gradually increases from Z = OCH_3 to Z = CN 839
 but dips slightly for Z = NO_2 . A similar trend for G_{elec} is found, 840
 although the slope is considerably different. As a result, the 841
 lowest reaction barrier for Z = OCH_3 and Z = CH_3 leads to a 842

843 favorable electrophilic over nucleophilic pathway, whereas for
844 the other substrates a more favorable nucleophilic pathway is
845 predicted. The empirical values used in the valence bond
846 model, therefore, predict reactivity trends in close agreement
847 with those found experimentally even though a slightly earlier
848 change from electrophilic to nucleophilic is found. Con-
849 sequently, the VB diagram and VB analysis predicts a
850 mechanistic change for substrate sulfoxidation by $[\text{Mn}(\text{O})-$
851 $(\text{H}_8\text{Cz})(\text{CN})]^-$ upon replacing the para substituent from a
852 strongly electron-donating group, such as OCH_3 , to a more
853 electron-withdrawing substituent like CN or NO_2 . This unique
854 profile is only found for the singlet spin reaction pathway via
855 ${}^1\text{TS}_{\text{SO}_2}$ and not found for the triplet spin barriers. Therefore,
856 the change in mechanism from nucleophilic to electrophilic is
857 clear evidence of singlet spin reactivity without crossover to a
858 higher spin state surface. Thus, the experimental Hammett plot
859 represents the first example of proof of singlet spin reactivity
860 originating from a closed-shell singlet manganese(V)-oxo
861 complex.

862 Finally, note that computational modeling proposed spin-
863 selective reactivity for several examples previously. Thus,
864 substrate sulfoxidation by iron(IV)-oxo porphyrin cation
865 radical complexes generally gives lower barriers on the doublet
866 spin state than on the quartet spin state and thereby gives spin-
867 selective reactivities with different reaction trends.^{38,50}
868 Furthermore, aromatic hydroxylation by iron(IV)-oxo por-
869 phyrin cation radical models often gives spin-selective reactivity
870 too through a rate-determining electrophilic reaction step
871 where two electrons are transferred from substrate to oxidant
872 and hence gives different barrier heights on each spin state
873 surface.⁵¹ As such, these systems may very well give different
874 Hammett plots for substrate sulfoxidation and aromatic
875 hydroxylation, but future studies will need to be done to
876 establish these details.

877 ■ CONCLUSION

878 A series of detailed computational studies has been performed
879 on the reaction mechanism of $[\text{Mn}(\text{O})(\text{H}_8\text{Cz})(\text{CN})]^-$ with
880 para-Z-substituted thioanisole substrates. This is a rare example
881 where a change in reaction mechanism is observed upon
882 changing the para-Z substituent of thioanisoles. Our detailed
883 computational analysis provides evidence that this mechanistic
884 change can only happen on the singlet spin state surface in
885 barrier ${}^1\text{TS}_{\text{SO}_2}$, whereas no mechanistic change is expected on
886 the triplet spin state surface. The experimental Hammett plot
887 provides a means to identify the reactive spin state of a high-
888 valent manganese-oxo complex and highlights a low-spin
889 reactivity pathway.

890 A range of density functional and ab initio methods up to the
891 NEVPT2:CAS(12,11) level of theory have been applied and
892 tested the models and methods. The NEVPT2:CAS calcu-
893 lations predict well-separated singlet and triplet spin states in
894 the reactant structures by well over 8–10 kcal mol⁻¹. Although
895 during the reaction mechanism we find close-lying singlet and
896 triplet spin state surfaces with an accessible spin-crossing point
897 lower in energy than the sulfoxidation barriers, actually the
898 spin-orbit coupling constant is very small. Therefore, theory
899 predicts it to be unlikely that a spin state crossing from the
900 singlet to the triplet spin state will take place. The
901 computational rate constants give a V-shaped Hammett plot
902 for para-Z-substituted sulfoxidation reactions in agreement with
903 experiment. The mechanism and ligand and substituent effects
904 are generalized with thermochemical cycles and valence bond

theory, which confirm the hypothesis and explain the change in
reaction mechanism from nucleophilic to electrophilic. 906

■ ASSOCIATED CONTENT

Supporting Information

The Supporting Information is available free of charge on the
ACS Publications website at DOI: 10.1021/jacs.6b05027. 910

Computational tables with group spin densities and
charges and absolute and relative energies of all
structured discussed here as well as Cartesian coordinates
of optimized geometries (PDF) 914

■ AUTHOR INFORMATION

Corresponding Authors

*dpg@jhu.edu 916

*sam.devisser@manchester.ac.uk 918

Present Address

[§]School of Chemistry, Cardiff University, Main Building, Park
Place, Cardiff CF10 3AT, United Kingdom. 920

Author Contributions

The manuscript was written through contributions of all
authors. All authors have given approval to the final version of
the manuscript. 925

Notes

The authors declare no competing financial interest. 927

■ ACKNOWLEDGMENTS

S.P.d.V. thanks the National Service of Computational
Chemistry Software for CPU time. This work was supported
by the NIH (GM101153) to D.P.G. F.G.C.R. thanks the
Conacyt Mexico for a studentship. 932

■ REFERENCES

- (1) See, e.g.: (a) Solomon, E. I.; Brunold, T. C.; Davis, M. I.; Kemsley, J. N.; Lee, S. K.; Lehnert, N.; Neese, F.; Skulan, A. J.; Yang, Y. S.; Zhou, J. *Chem. Rev.* **2000**, *100*, 235–349. (b) Bugg, T. D. H. *Curr. Opin. Chem. Biol.* **2001**, *5*, 550–555. (c) Ryle, M. J.; Hausinger, R. P. *Curr. Opin. Chem. Biol.* **2002**, *6*, 193–201. (d) Costas, M.; Mehn, M. P.; Jensen, M. P.; Que, L., Jr. *Chem. Rev.* **2004**, *104*, 939–986. (e) Abu-Omar, M. M.; Loaiza, A.; Hontzeas, N. *Chem. Rev.* **2005**, *105*, 2227–2252. (f) Bruijninx, P. C. M.; van Koten, G.; Klein Gebbink, R. J. M. *Chem. Soc. Rev.* **2008**, *37*, 2716–2744. (g) Kryatov, S. V.; Rybak-Akimova, E. V.; Schindler, S. *Chem. Rev.* **2005**, *105*, 2175–2226. (2) (a) Ortiz de Montellano, P. R. *Chem. Rev.* **2010**, *110*, 932–948. (b) Guengerich, F. P. *Chem. Res. Toxicol.* **2001**, *14*, 611–650. (c) Munro, A. W.; Girvan, H. M.; McLean, K. J. *Nat. Prod. Rep.* **2007**, *24*, 585–609. (d) Li, D.; Wang, Y.; Han, K. *Coord. Chem. Rev.* **2012**, *256*, 1137–1150. (3) (a) Meunier, B.; de Visser, S. P.; Shaik, S. *Chem. Rev.* **2004**, *104*, 3947–3980. (b) Denisov, I. G.; Makris, T. M.; Sligar, S. G.; Schlichting, I. *Chem. Rev.* **2005**, *105*, 2253–2277. (c) Rittle, J.; Green, M. T. *Science* **2010**, *330*, 933–937. (4) (a) Krebs, C.; Galonić Fujimori, D.; Walsh, C. T.; Bollinger, J. M., Jr. *Acc. Chem. Res.* **2007**, *40*, 484–492. (b) Nam, W. *Acc. Chem. Res.* **2007**, *40*, 522–531. (5) (a) Shaik, S.; de Visser, S. P.; Ogliaro, F.; Schwarz, H.; Schröder, D. *Curr. Opin. Chem. Biol.* **2002**, *6*, 556–567. (b) de Visser, S. P.; Ogliaro, F.; Harris, N.; Shaik, S. *J. Am. Chem. Soc.* **2001**, *123*, 3037–3047. (c) de Visser, S. P.; Ogliaro, F.; Sharma, P. K.; Shaik, S. *Angew. Chem., Int. Ed.* **2002**, *41*, 1947–1951. (6) See, e.g.: (a) Comba, P.; Kerscher, M. *Coord. Chem. Rev.* **2009**, *253*, 564–574. (b) Fukuzumi, S. *Coord. Chem. Rev.* **2013**, *257*, 1564–1575. (c) Ray, K.; Pfaff, F. F.; Wang, B.; Nam, W. *J. Am. Chem. Soc.* **963**

- 964 **2014**, 136, 13942–13958. (d) Que, L., Jr; Tolman, W. B. *Nature* **2008**, 965 455, 333–340.
- 966 (7) (a) Nam, W.; Lee, Y.-M.; Fukuzumi, S. *Acc. Chem. Res.* **2014**, 47, 967 1146–1154. (b) McDonald, A.; Que, L., Jr *Coord. Chem. Rev.* **2013**, 968 257, 414–428. (c) Ryabov, A. D. *Adv. Inorg. Chem.* **2013**, 65, 117–969 163.
- 970 (8) (a) Neu, H.; Baglia, R. A.; Goldberg, D. P. *Acc. Chem. Res.* **2015**, 971 48, 2754–2764. (b) Chen, Z.; Yin, G. *Chem. Soc. Rev.* **2015**, 44, 1083–972 1100.
- 973 (9) (a) Usharani, D.; Janardanan, D.; Li, S.; Shaik, S. *Acc. Chem. Res.* 974 **2013**, 46, 471–482. (b) Holland, P. L. *Acc. Chem. Res.* **2015**, 48, 975 1696–1702.
- 976 (10) (a) Hirao, H.; Kumar, D.; Que, L., Jr; Shaik, S. *J. Am. Chem. Soc.* 977 **2006**, 128, 8590–8606. (b) Mandal, D.; Ramanan, R.; Usharani, D.; 978 Janardanan, D.; Wang, B.; Shaik, S. *J. Am. Chem. Soc.* **2015**, 137, 722–979 733. (c) Mandal, D.; Shaik, S. *J. Am. Chem. Soc.* **2016**, 138, 2094–980 2097.
- 981 (11) (a) Liu, H. Y.; Zhou, H.; Liu, L. Y.; Ying, X.; Jiang, H. F.; Chang, 982 C. K. *Chem. Lett.* **2007**, 36, 274–275. (b) Jin, N.; Ibrahim, M.; Spiro, 983 T. G.; Groves, J. T. *J. Am. Chem. Soc.* **2007**, 129, 12416–12417.
- 984 (12) Prokop, K. A.; de Visser, S. P.; Goldberg, D. P. *Angew. Chem.,* 985 *Int. Ed.* **2010**, 49, 5091–5095.
- 986 (13) Janardanan, D.; Usharani, D.; Shaik, S. *Angew. Chem., Int. Ed.* 987 **2012**, 51, 4421–4425.
- 988 (14) (a) Neu, H. M.; Yang, T.; Baglia, R. A.; Yosca, T. H.; Green, M. 989 T.; Quesne, M. G.; de Visser, S. P.; Goldberg, D. P. *J. Am. Chem. Soc.* 990 **2014**, 136, 13845–13852. (b) Neu, H. M.; Quesne, M. G.; Yang, T.; 991 Prokop-Prigge, K. A.; Lancaster, K. M.; Donohoe, J.; DeBeer, S.; de 992 Visser, S. P.; Goldberg, D. P. *Chem. - Eur. J.* **2014**, 20, 14584–14588.
- 993 (15) (a) Neese, F. *Comput. Mol. Sci.* **2012**, 2, 73–78. (b) Frisch, M. 994 J.; Trucks, G. W.; Schlegel, H. B.; Scuseria, G. E.; Robb, M. A.; 995 Cheeseman, J. R.; Scalmani, G.; Barone, V.; Mennucci, B.; Petersson, 996 G. A.; Nakatsuji, H.; Caricato, M.; Li, X.; Hratchian, H. P.; Izmaylov, 997 A. F.; Bloino, J.; Zheng, G.; Sonnenberg, J. L.; Hada, M.; Ehara, M.; 998 Toyota, K.; Fukuda, R.; Hasegawa, J.; Ishida, M.; Nakajima, T.; Honda, 999 Y.; Kitao, O.; Nakai, H.; Vreven, T.; Montgomery, Jr, J. A.; Peralta, J. 1000 E.; Ogliaro, F.; Bearpark, M.; Heyd, J. J.; Brothers, E.; Kudin, K. N.; 1001 Staroverov, V. N.; Keith, T.; Kobayashi, R.; Normand, J.; Raghavachari, 1002 K.; Rendell, A.; Burant, J. C.; Iyengar, S. S.; Tomasi, J.; Cossi, M.; 1003 Rega, N.; Millam, J. M.; Klene, M.; Knox, J. E.; Cross, J. B.; Bakken, V.; 1004 Adamo, C.; Jaramillo, J.; Gomperts, R.; Stratmann, R. E.; Yazyev, O.; 1005 Austin, A. J.; Cammi, R.; Pomelli, C.; Ochterski, J. W.; Martin, R. L.; 1006 Morokuma, K.; Zakrzewski, V. G.; Voth, G. A.; Salvador, P.; 1007 Dannenberg, J. J.; Dapprich, S.; Daniels, A. D.; Farkas, O.; 1008 Foresman, J. B.; Ortiz, J. V.; Cioslowski, J.; Fox, D. J. *Gaussian 09*, 1009 Revision C.01; Gaussian, Inc.: Wallingford, CT, 2010.
- 1010 (16) Sainna, M. A.; Sil, D.; Sahoo, D.; Martin, B.; Rath, S. P.; Comba, 1011 P.; de Visser, S. P. *Inorg. Chem.* **2015**, 54, 1919–1930.
- 1012 (17) Sainna, M. A.; Kumar, S.; Kumar, D.; Fornarini, S.; Crestoni, M. 1013 E.; de Visser, S. P. *Chem. Sci.* **2015**, 6, 1516–1529.
- 1014 (18) (a) Becke, A. D. *J. Chem. Phys.* **1993**, 98, 5648–5652. (b) Lee, 1015 C.; Yang, W.; Parr, R. G. *Phys. Rev. B: Condens. Matter Mater. Phys.* 1016 **1988**, 37, 785–789.
- 1017 (19) (a) Hay, P. J.; Wadt, W. R. *J. Chem. Phys.* **1985**, 82, 270–283. 1018 (b) Hehre, W. J.; Ditchfield, R.; Pople, J. A. *J. Chem. Phys.* **1972**, 56, 1019 2257–2262.
- 1020 (20) Grimme, S.; Antony, J.; Ehrlich, S.; Krieg, H. *J. Chem. Phys.* 1021 **2010**, 132, 154104.
- 1022 (21) Tao, J.; Perdew, J. P.; Staroverov, V. N.; Scuseria, G. E. *Phys.* 1023 *Rev. Lett.* **2003**, 91, 146401.
- 1024 (22) Klamt, A.; Schuurmann, G. *J. Chem. Soc., Perkin Trans. 2* **1993**, 1025 799–805.
- 1026 (23) (a) Becke, A. D. *Phys. Rev. A: At, Mol., Opt. Phys.* **1988**, 38, 1027 3098–3100. (b) Perdew, J. P. *Phys. Rev. B: Condens. Matter Mater.* 1028 *Phys.* **1986**, 33, 8822–8824.
- 1029 (24) Perdew, J. P.; Burke, K.; Ernzerhof, M. *Phys. Rev. Lett.* **1996**, 77, 1030 3865–3868.
- 1031 (25) Adamo, C.; Barone, V. *J. Chem. Phys.* **1999**, 110, 6158–6169.
- 1032 (26) van Wuellen, C. *J. Chem. Phys.* **1998**, 109, 392–399.
- (27) Pantazis, D. A.; Chen, X. Y.; Landis, C. R.; Neese, F. *J. Chem. Theory Comput.* **2008**, 4, 908–915. 1033
- (28) <ftp.chemie.uni-karlsruhe.de/pub/basen>. 1034
- (29) Hess, B. A.; Marian, C. M.; Wahlgren, U.; Gropen, O. *Chem. Phys. Lett.* **1996**, 251, 365–371. 1035
- (30) (a) Ghosh, A.; Taylor, P. R. *Curr. Opin. Chem. Biol.* **2003**, 7, 1036 113–124. (b) de Visser, S. P.; Stillman, M. J. *Int. J. Mol. Sci.* **2016**, 17, 1037 519–544. 1038
- (31) (a) de Visser, S. P.; Quesne, M. G.; Martin, B.; Comba, P.; 1039 1040 Ryde, U. *Chem. Commun.* **2014**, 50, 262–282. (b) Sallmann, M.; 1041 Kumar, S.; Chernev, P.; Nehr Korn, J.; Schnegg, A.; Kumar, D.; Dau, 1042 H.; Limberg, C.; de Visser, S. P. *Chem. - Eur. J.* **2015**, 21, 7470–7479. 1043
- (32) Janesko, B. G. *Int. J. Quantum Chem.* **2013**, 113, 83–88. 1044
- (33) Hull, J. F.; Balcells, D.; Sauer, E. L. O.; Raynaud, C.; Brudvig, G. 1045 W.; Crabtree, R. H.; Eisenstein, O. *J. Am. Chem. Soc.* **2010**, 132, 7605–1046 7616. 1047
- (34) de Visser, S. P.; Shaik, S.; Sharma, P. K.; Kumar, D.; Thiel, W. J. 1048 *Am. Chem. Soc.* **2003**, 125, 15779–15788. 1049
- (35) Leeladee, P.; Baglia, R. A.; Prokop, K. A.; Latifi, R.; de Visser, S. 1050 P.; Goldberg, D. P. *J. Am. Chem. Soc.* **2012**, 134, 10397–10400. 1051
- (36) (a) Postils, V.; Company, A.; Solà, M.; Costas, M.; Luis, J. M. 1052 *Inorg. Chem.* **2015**, 54, 8223–8236. (b) Hirao, H. *J. Phys. Chem. A* 1053 **2011**, 115, 9308–9313. 1054
- (37) (a) Prokop, K. A.; Neu, H. M.; de Visser, S. P.; Goldberg, D. P. 1055 *J. Am. Chem. Soc.* **2011**, 133, 15874–15877. (b) Takahashi, A.; Yamaki, 1056 D.; Ikemura, K.; Kurahashi, T.; Ogura, T.; Hada, M.; Fujii, H. *Inorg.* 1057 *Chem.* **2012**, 51, 7296–7305. 1058
- (38) (a) Kumar, D.; Sastry, G. N.; de Visser, S. P. *Chem. - Eur. J.* 1059 **2011**, 17, 6196–6205. (b) Kumar, S.; Faponle, A. S.; Barman, P.; 1060 Vardhaman, A. K.; Sastri, C. V.; Kumar, D.; de Visser, S. P. *J. Am.* 1061 *Chem. Soc.* **2014**, 136, 17102–17115. 1062
- (39) Harvey, J. N.; Aschi, M.; Schwarz, H.; Koch, W. *Theor. Chem. Acc.* **1998**, 99, 95–98. 1063
- (40) Kumar, D.; Latifi, R.; Kumar, S.; Rybak-Akimova, E. V.; Sainna, 1064 M. A.; de Visser, S. P. *Inorg. Chem.* **2013**, 52, 7968–7979. 1065
- (41) (a) Faponle, A. S.; Quesne, M. G.; de Visser, S. P. *Chem. - Eur. J.* 1066 **2016**, 22, 5478–548. (b) Barman, P.; Upadhyay, P.; Faponle, A. S.; 1067 Kumar, J.; Nag, S. S.; Kumar, D.; Sastri, C. V.; de Visser, S. P. *Angew.* 1068 *Chem., Int. Ed.* **2016**, in press, DOI: 10.1002/anie.201604412. 1069
- (42) (a) Kumar, D.; de Visser, S. P.; Shaik, S. *J. Am. Chem. Soc.* **2003**, 1070 125, 13024–1302. (b) Kumar, D.; de Visser, S. P.; Sharma, P. K.; 1071 Cohen, S.; Shaik, S. *J. Am. Chem. Soc.* **2004**, 126, 1907–1920. 1072
- (43) (a) Gross, Z.; Nimri, S. *Inorg. Chem.* **1994**, 33, 1731–1732. 1073 (b) Czarniecki, K.; Nimri, S.; Gross, Z.; Proniewicz, L. M.; Kincaid, J. 1074 *R. J. Am. Chem. Soc.* **1996**, 118, 2929–2935. (c) Song, W. J.; Ryu, Y. 1075 O.; Song, R.; Nam, W. *JBIC, J. Biol. Inorg. Chem.* **2005**, 10, 294–304. 1076
- (d) Crestoni, M. E.; Fornarini, S.; Lanucara, F. *Chem. - Eur. J.* **2009**, 1077 15, 7863–7866. 1078
- (44) (a) Sastri, C. V.; Lee, J.; Oh, K.; Lee, Y. J.; Lee, J.; Jackson, T. A.; 1079 Ray, K.; Hirao, H.; Shin, W.; Halfen, J. A.; Kim, J.; Que, L., Jr; Shaik, 1080 S.; Nam, W. *Proc. Natl. Acad. Sci. U. S. A.* **2007**, 104, 19181–19186. 1081 (b) Jackson, T. A.; Rohde, J.-U.; Seo, M. S.; Sastri, C. V.; DeHont, R.; 1082 Stubna, A.; Ohta, T.; Kitagawa, T.; Münck, E.; Nam, W.; Que, L., Jr *J.* 1083 *Am. Chem. Soc.* **2008**, 130, 12394–12407. 1084
- (45) (a) de Visser, S. P.; Ogliaro, F.; Sharma, P. K.; Shaik, S. *J. Am.* 1085 *Chem. Soc.* **2002**, 124, 11809–11826. (b) de Visser, S. P. *Chem. - Eur. J.* 1086 **2006**, 12, 8168–8177. (c) de Visser, S. P.; Latifi, R.; Tahsini, L.; Nam, 1087 W. *Chem. - Asian J.* **2011**, 6, 493–504. 1088
- (46) (a) Takahashi, A.; Kurahashi, T.; Fujii, H. *Inorg. Chem.* **2011**, 50, 1089 6922–6928. (b) Cong, Z.; Kurahashi, T.; Fujii, H. *Angew. Chem., Int.* 1090 *Ed.* **2011**, 50, 9935–9939. 1091
- (47) Mayer, J. M. *J. Phys. Chem. Lett.* **2011**, 2, 1481–1489. 1092
- (48) (a) Shaik, S.; Kumar, D.; de Visser, S. P. *J. Am. Chem. Soc.* **2008**, 1093 130, 10128–10140. (b) de Visser, S. P. *J. Am. Chem. Soc.* **2010**, 132, 1094 1087–1097. (c) Kumar, D.; Karamzadeh, B.; Sastry, G. N.; de Visser, 1095 S. P. *J. Am. Chem. Soc.* **2010**, 132, 7656–7667. 1096
- (49) Quesne, M. G.; Senthilnathan, D.; Singh, D.; Kumar, D.; 1097 Maldivi, P.; Sorokin, A. B.; de Visser, S. P. *ACS Catal.* **2016**, 6, 2230–1100 2243. 1101

- 1102 (50) (a) Kumar, D.; de Visser, S. P.; Sharma, P. K.; Hirao, H.; Shaik,
1103 S. *Biochemistry* **2005**, *44*, 8148–8158. (b) Vardhaman, A. K.; Barman,
1104 P.; Kumar, S.; Sastri, C. V.; Kumar, D.; de Visser, S. P. *Angew. Chem*,
1105 *Int. Ed.* **2013**, *52*, 12288–12292.
- 1106 (51) (a) de Visser, S. P.; Shaik, S. *J. Am. Chem. Soc.* **2003**, *125*, 7413–
1107 7424. (b) Faponle, A. S.; Quesne, M. G.; Sastri, C. V.; Banse, F.; de
1108 Visser, S. P. *Chem. - Eur. J.* **2015**, *21*, 1221–1236.